INTERNATIONAL JOURNAL FOR NUMERICAL AND ANALYTICAL METHODS IN GEOMECHANICS, VOL. 21, 687–719 (1997)

DEFORMATION ANALYSIS OF SHALLOW PENETRATION IN CLAY

C. SAGASETA[1,*], A. J. WHITTLE[2] AND M. SANTAGATA[2]

[1] *University of Cantabria, 39005 Santander, Spain*
[2] *Massachusetts Institute of Technology, Cambridge, MA02139, USA*

SUMMARY

A new method of analysis is described for estimating the deformations and strains caused by shallow undrained penetration of piles and caissons in clay. The formulation combines previous analyses for steady, deep penetration,[1] with methods used to compute soil deformations due to near-surface ground loss,[2] and is referred to as the Shallow Strain Path Method (SSPM). Complete analytical solutions for the velocity and strain rates are given for a planar wall, an axisymmetric, closed-ended pile and unplugged, open-ended pile geometries. In these examples, the analyses consider a single source penetrating through the soil at a constant rate, generating a family of penetrometers with rounded tips, referred to as simple wall, pile and tube geometries. Soil deformations and strains are obtained by integrating the velocity and strain rates along the particle paths.

The transition from shallow to deep penetration is analysed in detail. Shallow penetration causes heave at the ground surface, while settlements occur only in a thin veneer of material adjacent to the shaft and in a bulb-shaped region around the tip. The size of this region increases with the embedment depth. Deformations inside an open-ended pile/caisson are affected significantly by details of the simple tube wall geometry. © 1997 by John Wiley & Sons, Ltd.

Int. J. Numer. Anal. Meth. Geomech., Vol. 21, 687–719 (1997)
(No. of Figures: 17 No. of Tables: 0 No. of Refs: 21)

Key words: deformation analysis; Shallow Strain Path Method (SSPM); penetration of clay

1. INTRODUCTION

There are many practical geotechnical problems associated with penetration of clays by foundation elements (piles, caissons, spudcans, etc.), *in situ* test devices (piezocone, dilatometer, etc.) or samplers.

The theoretical analysis of penetration is particularly difficult due to the high gradients of the field variables (displacements, stresses, strains and pore pressures) around the penetrometer, the large deformations and strains in the soil, the complex constitutive behaviour of soils, and non-linear penetrometer–soil interface characteristics. Baligh[1] proposed an approximate framework of analysis known as the Strain Path Method (SPM) which assumes that the soil deformations and strains caused by undrained, steady, 'deep' penetration in clay are essentially independent of its

Correspondence to: C. Sagaseta, Universidad de Cantabria, OCITTYM, Division de Ingenieria del Terreno, 39005 Santander, Spain.

Contract grant sponsor: DGICYT, Spain; contract grant no: 93-204.

CCC 0363–9061/97/100687–33$17.50

Received 5 August 1996
Revised 20 January 1997

shear resistance and can be estimated from the irrotational flow of an ideal fluid. Strain path analyses have been applied to cone penetrometers, cylindrical closed and open-ended piles, and thin plates.[3–5]

The restriction of the strain path analyses to conditions of steady, deep penetration can be acceptable for calculating strains near the tip, but has no physical meaning for far field conditions, where the presence of the ground surface is likely to affect soil deformations. For example, in the SPM analysis of pile penetration, all soil elements undergo net downward movements, whereas there are many published field observations of ground surface heave caused by pile driving. Further complications arise where the total penetration depth is of similar magnitude to the diameter of an open-ended pile, which is typical of caisson anchors proposed for offshore tension leg platforms.[6,7]

In order to address these limitations, this paper presents a modified strain path analysis,[8] which explicitly includes the effects of the stress free ground surface. This Shallow Strain Path Method (SSPM) is applied to the deformations and strains caused by the penetration of an infinitely long wall, a closed-ended, cylindrical simple pile (cf. Reference 9), and a simple tube (open-ended caisson, cf. Reference 10).

2. METHOD OF ANALYSIS

2.1. The Strain Path Method

The Strain Path Method (SPM) is based on experimental observations (e.g. References 11 and 12) which indicate that soil deformations caused by deep penetration of rigid tools are similar in different soils, although the penetration resistance (and hence, soil stresses) can be radically different.[13] Hence, the deformations can be estimated, with a reasonable degree of accuracy, independent of the stress–strain–strength properties of a particular soil. In the subsequent development of the method, soil deformations were estimated using velocity fields from potential theory (where the material properties correspond to an ideal, incompressible and inviscid fluid).

Using this approximation, different penetrometer geometries can be modelled through combinations of sources and sinks (e.g. References 5 and 13) or other surface mapping techniques (panel/boundary element methods, e.g. Reference 14). However, the analysis of a single source provides a good understanding of the deformation mechanisms.[9] The resulting penetrometer shape is referred to as a 'simple pile' in the case of a 3-D spherical source (point source), a 'simple wall', in a plane strain case (line source), or a 'simple tube' if a ring source is used.

For steady, deep penetration it is convenient to change the frame of reference and consider the steady flow of soil around a stationary penetrometer (fixed source of constant intensity) as shown in Figure 1. For the 'simple' penetrometer geometries, the velocity and strain rate components can be obtained in closed-form expressions, while the displacements and strains are solved by numerical integration along the streamlines.

Once the strain paths of individual soil elements are known, the material constitutive equations can be used to derive the effective soil stresses. For undrained penetration in clays, the constitutive equations can be represented using either total stresses (relating shear stresses and shear induced pore pressures to shear strains) or effective stress models. In either case, due to incompressibility, there is one stress component (either the excess pore pressure, Δu, or the mean normal stress, $\Delta\sigma$) that cannot be obtained from the stress–strain relations and must be solved from the equilibrium equations. In general, it is not possible to match all of the equilibrium equations with a single unknown function (i.e. field of Δu or $\Delta\sigma$). A unique solution for this stress component is only possible if the strain field (derived for an inviscid fluid) is exact.[15,16]

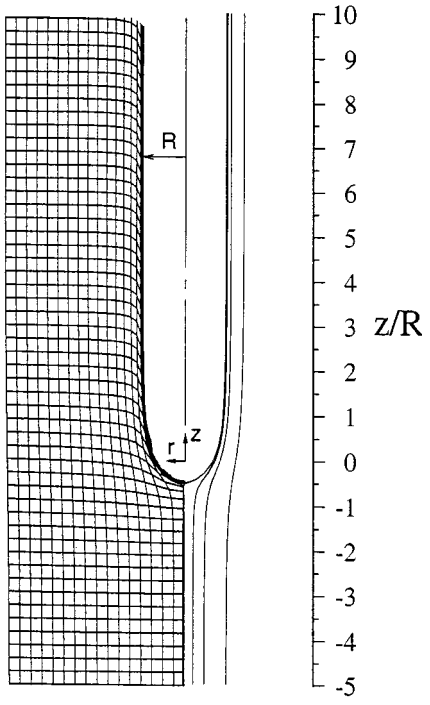

Figure 1. Strain Path Method for deep penetration viewed as a steady flow problem (after Baligh[1])

2.2. *Representation of free surface by image sources and sinks*

The presence of the ground surface causes an important change in the penetration problem conditions. The basic assumption that kinematic constraints govern the deformation is no longer valid. In fact, the ground surface is a traction-free boundary. Hence, the assumption that the deformation pattern in the soil can be approximated by solutions for an ideal fluid is more doubtful. As a result, any extension of the Strain Path Method to near-surface problems cannot be based exclusively on the inviscid fluid approach, and some consideration of the material shear stiffness is needed, either as a viscid fluid or as a solid.

Sagaseta[2] proposed a method for dealing with near-surface problems, where the principal focus was the prediction of ground deformations. The analysis assumed small strain conditions and formulated equations in terms of the final state of deformation (as opposed to the velocities occurring during penetration). According to this method, a point source discharging a volume, V, at some depth, $z = h$, below the ground surface can be modelled by the following three steps (Figure 2):

1. The ground surface is ignored, and solutions are obtained for the displacements and strains corresponding to a source, S, within an infinite, full space.
2. A sink, S', absorbing an equal and opposite volume to the source (i.e. $-V$) is located at an elevation $z = -h$ above the ground surface. At points along the ground surface, $z = 0$

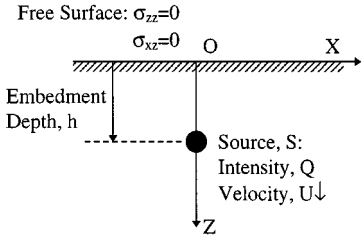

a) SSPM Representation of Shallow Penetration Problem

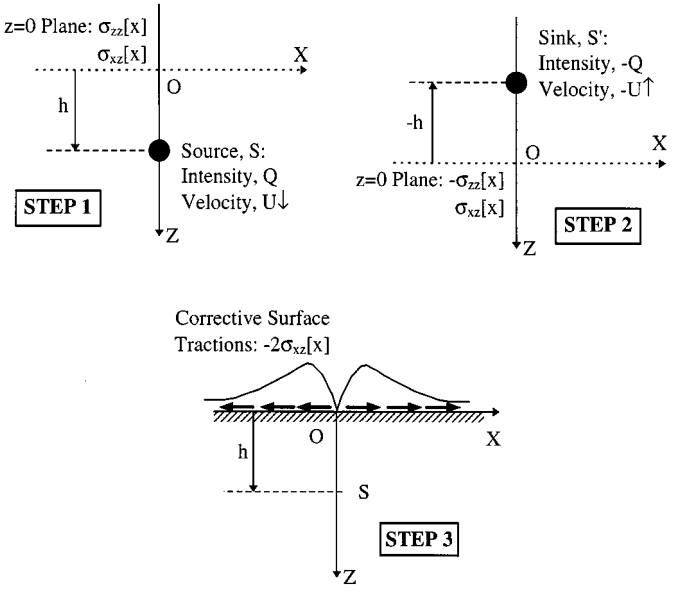

b) Equivalent Solution (Steps 1+2+3)

Figure 2. Conceptual model for simulation of penetration with stress-free surface

(plane of reflective symmetry), the virtual sink will cancel out the horizontal displacements due to the point source, but will double the vertical displacements.

For specified stress–strain properties of the medium, the source induces normal and shear tractions ($\sigma_{zz}[x], \sigma_{xz}[x]$) at all points along the ground surface, while the image sink generates components ($-\sigma_{zz}[x], \sigma_{xz}[x]$) along the same surface. Hence, by superimposing the source and image sink solutions, the ground surface experiences shear tractions of magnitude $2\sigma_{xz}[x]$ (Figure 2(b)).

3. In order to simulate a stress free surface, a distribution of corrective shear tractions is applied to the surface (Figure 2(b)). This involves the following steps: (a) evaluate the shear strains due to the source and image sink (S, S'; steps 1 and 2), (b) assume a given stress–strain behavior for the soil and hence, find the shear stresses associated with the strains occurring

at points along the ground surface; (c) apply a field of equal and opposite shear stresses (referred to as corrective shear tractions) over the surface and compute the distribution of shear strains which these generate in the underlying soil; and (d) add this strain distribution to the previous solutions from steps 1 and 2.

The calculation of corrective shear tractions in step 3(c) is based on analytic solutions for a homogeneous, linear, isotropic material. The resulting strains in step 3(d) are independent of the actual soil modulus (i.e., the modulus cancels out in performing steps 3(b) and 3(c)), and represent only a small fraction of the total shear strains computed around the pile tip and shaft. Hence, the assumption of linear stress–strain properties has very limited impact on results of the current analyses.

It is worth noting two additional points: (1) there are no vertical displacements of the ground surface due to the corrective surface tractions in step 3; and (2) the ground surface displacements are twice as large as the computed by the source S in an infinite space (i.e. solutions from step 1). This method has been applied to the analysis of ground movements caused by tunnelling,[2] pipe jacking,[17,18] and pile driving.[2,19] In all of these previous studies the analyses assume small strains.

2.3. *The Shallow Strain Path Method (SSPM)*

The presence of the ground surface means that penetration is no longer a steady-state process. Thus, there is no advantage in considering a reference system linked to the penetrating tool as used in the original Strain Path Method. Instead, the present analyses considers a source which penetrates downwards from the free surface.

The analyses follow the same methodology introduced by Sagaseta,[2] but the problem is now formulated in terms of the velocities of soil elements rather than their displacements. The resulting velocities and strain rates (from each of the three above steps) can then be integrated numerically along the particle paths, considering the changes in geometry. In principle, this approach can provide complete large strain solutions for the penetration problem. However, calculations of deformations due to the corrective surface tractions are based on small strain, elastic solutions for a system of horizontal shear forces that are always applied along the same horizontal plane. These approximations prevent reliable calculations of deformations and strains for soil elements initially located in a region close to both the ground surface and the path of the source. Numerical calculations for an axisymmetric simple pile define this no-go zone for soil elements with $r_0/R \leqslant 2{\cdot}0$ and $z_0/R \leqslant 0{\cdot}7$.

2.4. *Problem definition*

The penetrometer is represented by a source advancing from the ground surface at a constant speed, U. The depth reached at any time, t, is denoted as h, which increases until some final embedded length, L. Figure 3 shows the three 'simple' geometries considered:

Wall: Infinite line source discharging a volume q per unit time and length. The half-thickness of the wall is given by $w = q/(2U)$.

Axisymmetric, closed-ended pile: Point source discharging a volume Q per unit time. The radius of the pile is $R = \sqrt{Q/(\pi U)}$.

Axisymmetric open-ended pile or tube: Ring source of radius R, discharging a total volume Q per unit time. The wall half-thickness is $w = Q/(4\pi RU)$.

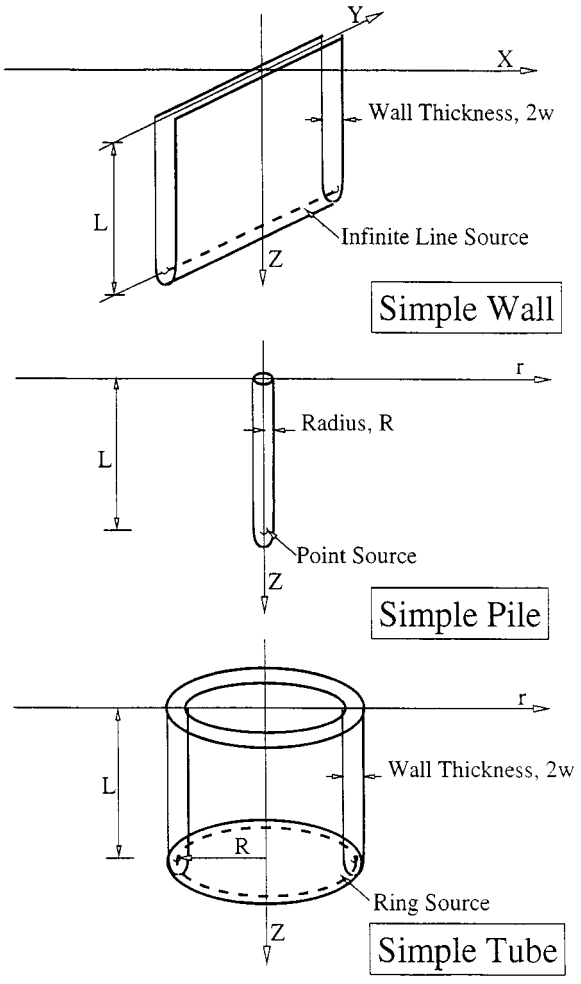

Figure 3. Problem geometry and notation

The analyses use cylindrical co-ordinate frames (r, θ, z) for the axisymmetric pile and tube geometries, and Cartesian co-ordinates (x, y, z) for the wall. The axes and notation are shown in Figure 3. Axis OZ is always taken downwards along the centreline, with the origin at the surface. All the formulation is presented either in the meridional section (rOZ) or the plane strain section (XOZ). The velocities and displacements are taken as positive in the positive directions of these axes. Normal strains are positive in compression, while opening of the angle XOZ gives positive shear strains (i.e. 'standard' soil mechanics sign convention).

2.5. Formulation

Appendix I gives complete expressions for the velocities (v_i) and strain rates $(\dot{\varepsilon}_{ij})$ at any point (x_i) for the source at depth $h(0 \leqslant h \leqslant L)$ for the wall, pile and tube geometries. In each case, the

solution (velocities and strain rates) is given as the sum of three components (Figure 2): (1) source, S; (2) image sink, S'; (3) corrective shear tractions.

Once the velocities and strain rates are defined, the displacements are obtained by integration of the velocities along the particle path. The position (x, z) of particle initially located at a point (x_0, z_0), when the source is at a depth h is:

$$\begin{Bmatrix} x(h) \\ z(h) \end{Bmatrix} = \begin{Bmatrix} x_0 \\ z_0 \end{Bmatrix} + \int_0^t \begin{Bmatrix} v_x(x,z,h) \\ v_z(x,z,h) \end{Bmatrix} \mathrm{d}t = \begin{Bmatrix} x_0 \\ z_0 \end{Bmatrix} + \int_0^h \begin{Bmatrix} v_x(x,z,h) \\ v_z(x,z,h) \end{Bmatrix} \frac{1}{U} \mathrm{d}h \tag{1}$$

The strains can then be obtained by integration of the strain rates along the particle paths:

$$\varepsilon_{ij} = \int_0^t \dot{\varepsilon}_{ij}(x,z,h)\,\mathrm{d}t = \int_0^h \frac{1}{U}\,\dot{\varepsilon}_{ij}(x,z,h)\,\mathrm{d}h. \tag{2}$$

Integration of equations (1) and (2) must be performed numerically, because the current co-ordinates (x, z) in the integrands are variable, defined precisely by integration of equation (1). If the changes of geometry are neglected (small strains), then the initial coordinates (x_0, z_0) can be used instead of the current ones in the expressions of (v_x, v_z) in the right-hand side of equation (1). Under this assumption, the solutions presented by Sagaseta[2] are obtained, leading to closed-form expressions in some cases, as shown in subsequent sections.

3. RESULTS FOR THE SIMPLE WALL

The plane strain simple wall is the simplest of the three penetrometer geometries considered in this paper. Appendix I shows the the velocity and strain rate components can all be obtained in closed-form expressions. Assuming small strain conditions, the velocities (equations 8(a), 10(a) and 12(a)) can also be integrated analytically over the full penetration depth of the wall $(0 \leqslant h \leqslant L)$, to obtain the soil displacements[2] as follows:

$$\begin{aligned} \delta_{x\mathrm{SS}} &= \frac{w}{\pi}\left[\tan^{-1}\left(\frac{z+L}{x}\right) - \tan^{-1}\left(\frac{z-L}{x}\right) + 2xz\left(\frac{1}{r_2^2} - \frac{1}{x^2+z^2}\right)\right] \\ \delta_{z\mathrm{SS}} &= -\frac{w}{\pi}\left[\ln\left(\frac{r_1 r_2}{x^2+z^2}\right) - 2z\left(\frac{z+L}{r_2^2} - \frac{z}{x^2+z^2}\right)\right] \end{aligned} \tag{3}$$

where $r_1 = \sqrt{x^2 + (z-L)^2}$, $r_2 = \sqrt{x^2 + (z+L)^2}$, and the subscript 'SS' refers to 'small strains'. At the surface ($z = 0$), equation (3) reduces to

$$\begin{aligned} \delta_{x\mathrm{SS}}(x,0) &= 2\,\frac{w}{\pi}\tan^{-1}(L/x) \\ \delta_{z\mathrm{SS}}(x,0) &= -\frac{w}{\pi}\ln[1 + (L/x)^2] \end{aligned} \tag{4}$$

The next paragraphs describe the deformations and strains of soil elements caused by penetration of the simple wall from the stress free surface down to a total embedment depth (of the line

source), $L/w = 10$, where w is the half-thickness of the wall. All the results are obtained for large strains, by numerical integration of equations (1) and (2).

3.1. Wall geometry

Figure 4 shows the wall geometry generated by the proposed SSPM analysis for shallow penetration to embedment depths, $L/w = 2, 5$, and 10. The solution for deep penetration ($L/w = \infty$)[10] is shown for comparison, with the source centred at $L/w = 10$. The tip geometry is practically identical in all cases. However, some differences are visible near the surface. For deep penetration, the wall thickness increases continuously with elevation above the tip, asymptotically approaching the reference dimension, w. In contrast, for the shallow penetration analyses, the wall reaches a maximum thickness at mid-depth, and then tapers slightly towards the ground surface. Narrowing of the wall section close to the ground surface is a consequence of two factors in the proposed SSPM analyses: (i) representation of the penetrometer geometry using a single source and image sink, and (ii) small strain approximations used in the corrective surface traction calculations (equation 12(a)).

The simple wall maintains its characteristic geometric form during penetration (rounded tip, shaft tapering towards the surface), while the actual dimensions of the shaft and tip (below the

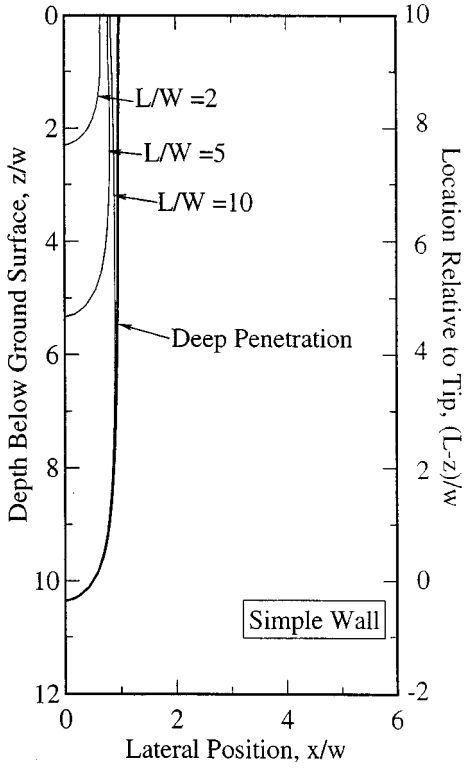

Figure 4. Effect of embedment depth on simple wall geometry

location of the line source) expand with the depth of penetration. At any given elevation within the soil, the wall thickness increases continuously as the source advances, and all soil elements undergo continuous outward lateral displacements at the penetration depth increases.

3.2. *Ground deformations*

Figure 5 shows the contours of the horizontal and vertical displacements for $L/w = 10$. Most of the soil mass undergoes net heave $\delta_z/w < 0$). The maximum heave, $\delta_z/w \approx -1{\cdot}3$, occurs close to the ground surface at a lateral distance $x/w = 1{\cdot}3$. The contour $\delta_z/w = 0$ (Figure 5b) delineates a zone of net settlement which is confined to a thin layer of soil close to the wall and to a tear shaped zone around the tip. The size of this zone is proportional to the wall length, L, extending about $\Delta z/L = 0{\cdot}3$ vertically ahead the source and $\Delta r/L = 0{\cdot}25$–$0{\cdot}3$ laterally, independent of the ratio L/w.

All of the soil mass experiences a net outward horizontal displacement ($\delta_x/w > 0$; Figure 5(a)). The largest horizontal displacements occur close to the wall at mid-embedment. In this zone, the displacements decrease with the distance to the wall, from a value of about 0·9 to 0·4–0·5, and then they show little attenuation with lateral distance. The shape of the δ_x/w contours closer to the ground surface reflects the tapering of the wall discussed above.

Figure 6 presents the displacement paths (x, z) of selected soil elements initially located at three different depths and eight lateral locations, as the wall penetrates from the surface to a total embedment, $L/w = 10$. This illustrates the transition from shallow to deep penetration which is achieved by the proposed SSPM analysis. There are significant differences in the overall pattern of deformations at the three elevations. At the mid-depth of the wall ($z_0/w = 5$), most of the soil (at $x/w > 0{\cdot}95$) undergoes a net upward displacement, however, the magnitudes of movements are much smaller than those close to the free surface ($z_0/w = 2$). The plane at $z_0/w = 9$ is located close to the wall tip at its final embedment, and shows net downward displacements extending laterally to $x/w \leqslant 1{\cdot}8$.

The results in Figure 6 also show that displacement paths of individual soil elements are quite complex and can involve one or more reversals in direction. While the tip is far above the soil element, lateral displacements remain small and the points move slightly upwards. As the wall tip passes the elevation of the soil element, large increments of outward lateral displacement occur; soil elements close to the axis are first forced downwards and then reverse direction as the tip penetrates below the elevation of these points. Continued penetration of the wall tip makes the outward lateral displacements increase, approaching asymptotic limit values; upward vertical displacements continue indefinitely with wall tip penetration, as expected for this plane strain geometry (i.e. there are no steady-state deformations for deep penetration of a simple wall). For most of the points, the paths show small upward movements at the start of penetration. This surprising behaviour can be traced to the corrective shear tractions and is not considered physically significant.

4. RESULTS FOR THE SIMPLE PILE

Appendix I shows that the velocity and strain rate expressions corresponding to Step 3 of the proposed SSPM analysis (i.e. equations (17a) and (17b)) are more complicated for the axisymmetric simple pile. Unlike the simple wall, these expressions cannot be integrated in closed-form, except at points along the stress-free ground ($z = 0$), where the displacements (for small strain

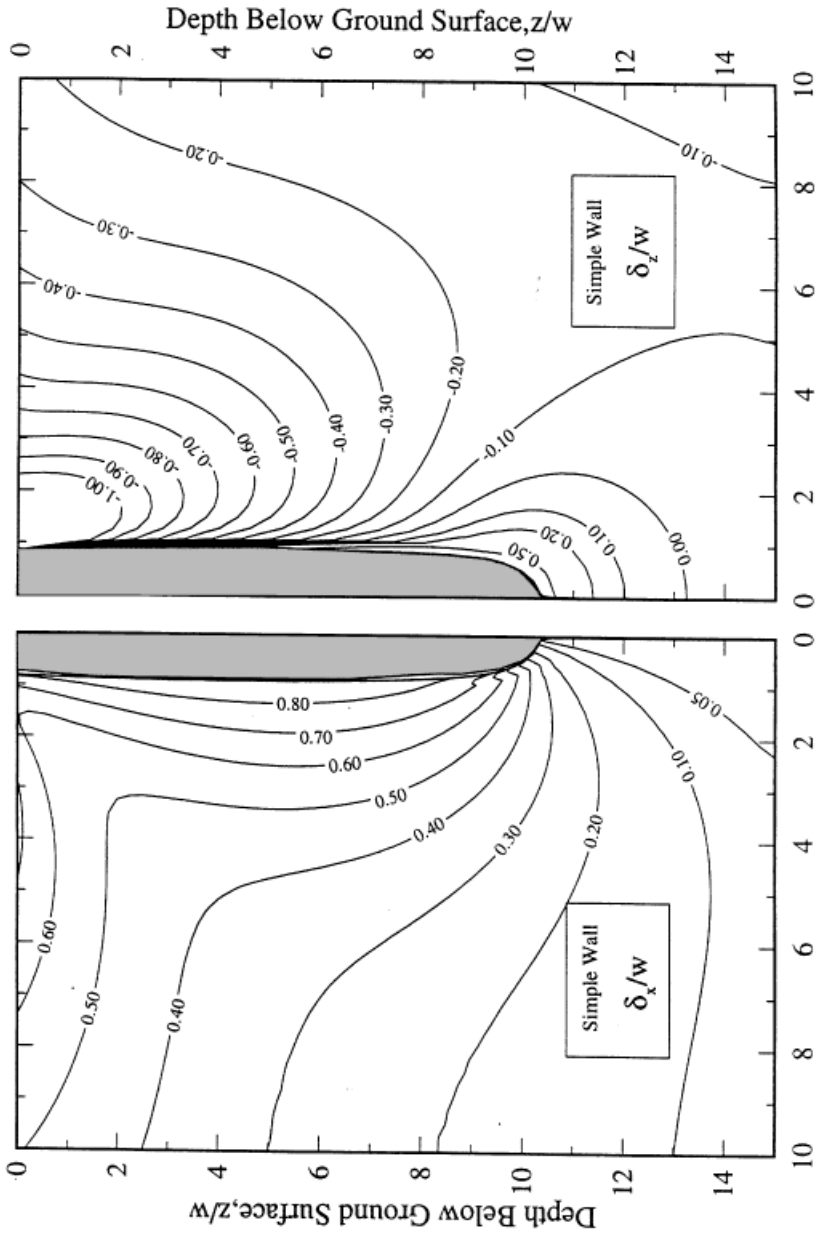

Figure 5. Displacement contours around simple wall with $L/w = 10$

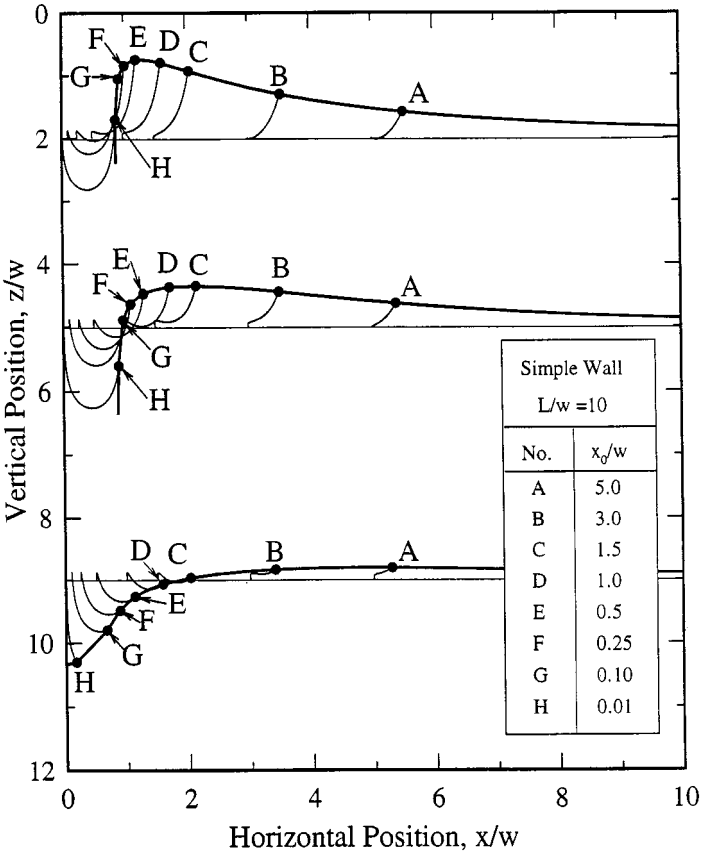

Figure 6. Deformation paths around simple wall with $L/w = 10$

assumptions) are:

$$\delta_{rss}(r,0) = \frac{R^2}{2}\frac{L}{r\sqrt{r^2+L^2}} = \frac{\Omega}{2\pi}\frac{L}{r\sqrt{r^2+L^2}}$$

$$\delta_{zss}(r,0) = -\frac{R^2}{2}\left(\frac{1}{r} - \frac{1}{\sqrt{r^2+L^2}}\right) = -\frac{\Omega}{2\pi}\left(\frac{1}{r} - \frac{1}{\sqrt{r^2+L^2}}\right) \tag{5}$$

where Ω is the cross-section area of the pile ($\Omega = \pi R^2$).

The calculations in the following sections are all based on numerical integration of equations (1) and (2) (large strains).

4.1. Pile geometry and ground deformations

Figures 7(a) and 7(b) summarize the total radial and vertical displacements of the soil as the pile reaches its final embedment depth, $L/R = 10$. The figures include the pile geometry and

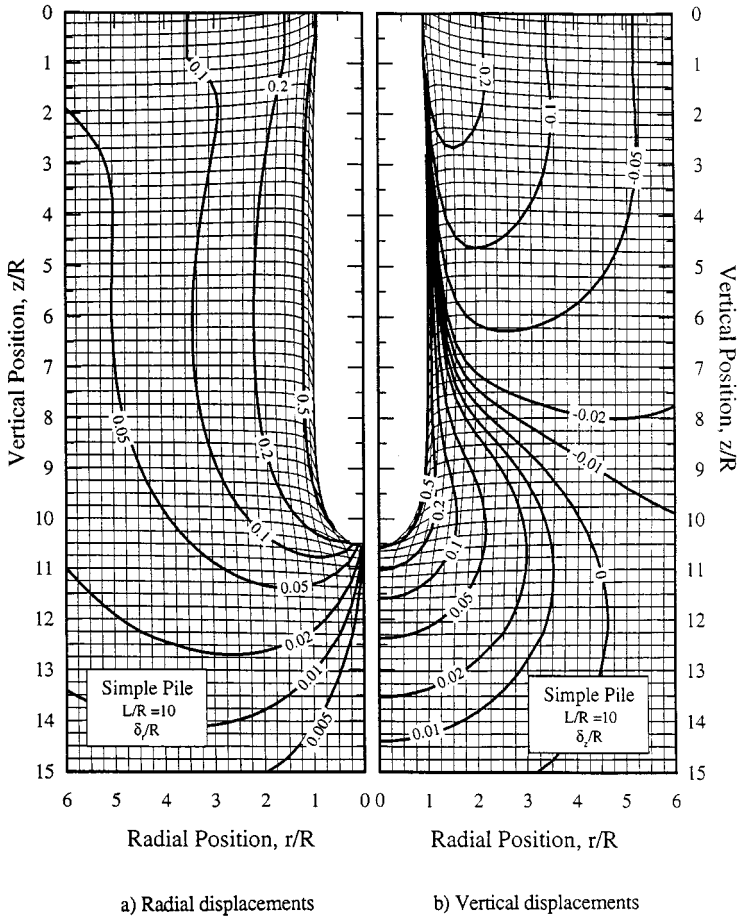

Figure 7. Soil deformations and displacement contours around simple pile with $L/R = 10$

distortion of an initially square grid ($\Delta r/R = \Delta z/R = 0{\cdot}25$) of soil elements, together with contours of selected values of δ_r/R and δ_z/R.

As in the case of the wall, the pile has a straight shaft over most of its embedded length, but it tapers noticeably at points closer to the free surface. At a given elevation within the soil, the radial dimension of the pile always expands with further penetration. This implies a continuous cavity expansion throughout the soil mass, and all points within the soil undergo a net outward radial displacement. Distortions of the pile shaft geometry are only significant for $z/R < 2$.

The tip shape of the pile does not vary significantly with penetration depth. In the vicinity of the tip, soil deformations are very similar to the distorted grid for deep penetration of the simple pile[1] with net downward displacements. As in the wall case, the settlements are restricted to a tear-shaped zone ahead of the pile tip and a thin annulus around the pile shaft. Further studies show that for pile length, L/R between 5 and 100, this settlement bulb expands in proportion to

the total penetration depth with $\Delta z/L = 0{\cdot}62$–$0{\cdot}70$, and $\Delta r/L = 0{\cdot}46$–$0{\cdot}47$. All the rest of the soil mass undergoes upward displacements. The maximum heave at the surface $\delta_z/R \approx -0{\cdot}6$) occurs very close to the pile shaft.

Figure 8 shows the deformation paths (r, z) of selected soil elements distributed radially (at $r_0/R = 0{\cdot}01$–$5{\cdot}0$) in three initial planes, $z_0/R = 1{\cdot}0, 5{\cdot}0$ and $9{\cdot}0$, as the simple pile penetrates to a total embedment depth $L/R = 10$, illustrating the transition from shallow to deep penetration. As a general trend, the displacement paths show the same stages as in the wall case (downwards, outwards and upwards). The first (downward) component dominates for points located near the pile axis. Near the surface, the third component is more important, resulting in a net heave.

In contrast to the wall geometry, vertical velocities diminish with continued penetration, and the displacements approach well defined asymptotic limits which are controlled by the initial depth and radial locations of the elements.

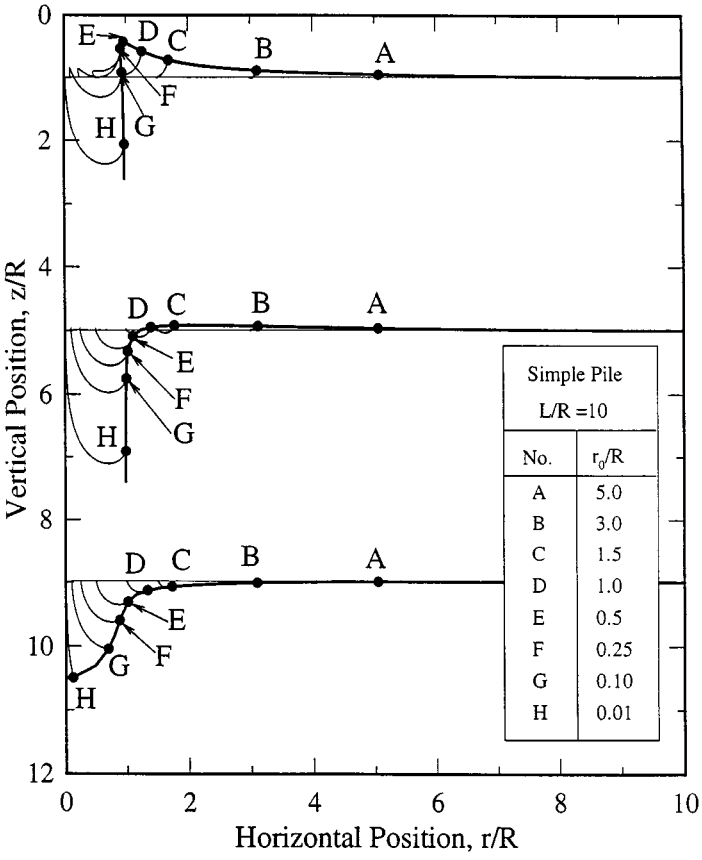

Figure 8. Deformation paths around simple pile with $L/R = 10$

4.2. Shear strains

Following Baligh,[1] the shear strains caused by undrained simple pile penetration can be conveniently characterized by three components:

$$E_1 = \varepsilon_{zz}, \quad E_2 = \frac{1}{\sqrt{3}}(\varepsilon_{rr} - \varepsilon_{\theta\theta}), \quad E_3 = \frac{2}{\sqrt{3}}\varepsilon_{rz} \tag{6}$$

These components correspond to triaxial, pressuremeter (cylindrical cavity expansion) and direct simple shear modes, respectively. Each of them contributes equally to the overall magnitude of the shear strain described by the second invariant of deviatoric strains, $E = (E_1^2 + E_2^2 + E_3^2)^{1/2}/\sqrt{2}$.

Figure 9(a)–9(d) compare contours of octahedral shear strain, E, caused by shallow pile penetration at embedment depths, $L/R = 2, 5$, and 10 with results of SPM analyses for deep penetration ($L/R = \infty$; Figure 9(d)). In all the cases, there is a zone of intense shearing ($E \geqslant 10\%$) which forms a sleeve around the pile with a thickness of about one pile radius around the shaft and half the radius ahead of the tip. The zone of intermediate strains, ($0{\cdot}1\% \leqslant E \leqslant 10\%$), which are sufficient to cause yielding of typical soft clays, expands continuously with penetration depth and hence, there is a progressive enlargement of the zone of soil yielding around the simple pile. This result has important implications for subsequent calculations of penetration resistance, soil stresses, etc.

Figures 10(a)–10(d) present the strain paths, E_2 vs. E_1 and E_2 vs. E_3 for selected soil elements at two elevations $z_0/R = 1{\cdot}0$ and $5{\cdot}0$, respectively. Two pairs of plots are shown for each elevation: (1) far field elements (A–D with $r_0/R = 1{\cdot}0$–$5{\cdot}0$) and (2) near field elements (E–H with $r_0/R = 0{\cdot}01$–$0{\cdot}5$). Several features of the strain paths, especially those at elevation $z_0/R = 5{\cdot}0$ (Figures 10(c) and 10(d)), are very similar to results predicted for deep penetration.[9]

The strain paths involve monotonically increasing cavity shear strains, E_2, while there are characteristic reversals in the triaxial (E_1) and simple shear (E_3) modes. Triaxial shearing (E_1) dominates the behaviour ahead of the pile tip (element H, $r_0/R = 0{\cdot}01$).

As the pile tip penetration proceeds, there is a general reduction in the magnitudes of E_1 and E_3 for the far field soil elements, such that the final state of strain is controlled by the magnitude of the cylindrical cavity expansion (E_2). However, in contrast to deep penetration, there are significant residual values (i.e. at the final embedment depth $L/R = 10$) of E_1 and E_3 at all radial locations.

For deeper points ($z_0/R > 5$), not shown in the figures, the strain paths are very similar to those located at $z_0/R = 5$ (Figures 10(c) and 10(d)), but they are curtailed as the pile reaches its final embedment at $L/R = 10$.

Regarding the shallow soil elements ($z_0/R = 1$), the points located close to the centreline and those far from the pile (i.e. G, H and A, B in Figures 10(a) and 10(b), respectively) also follow qualitatively similar strain paths to those at $z_0/R = 5$, although there are significant differences in the magnitudes of E_1 and E_3 at these two depths. However, intermediate soil elements, C–F (i.e. $r_0/R = 0{\cdot}25$–$1{\cdot}5$) show distinct differences from their counterparts at $z_0/R = 5$. The initial strain path involves a significant initial cavity contraction ($E_2 < 0$) associated with the unusual features of the displacement paths in this region, and the radial distribution of the surface heave produces residual values of simple shear strain $E_3 < 0$.

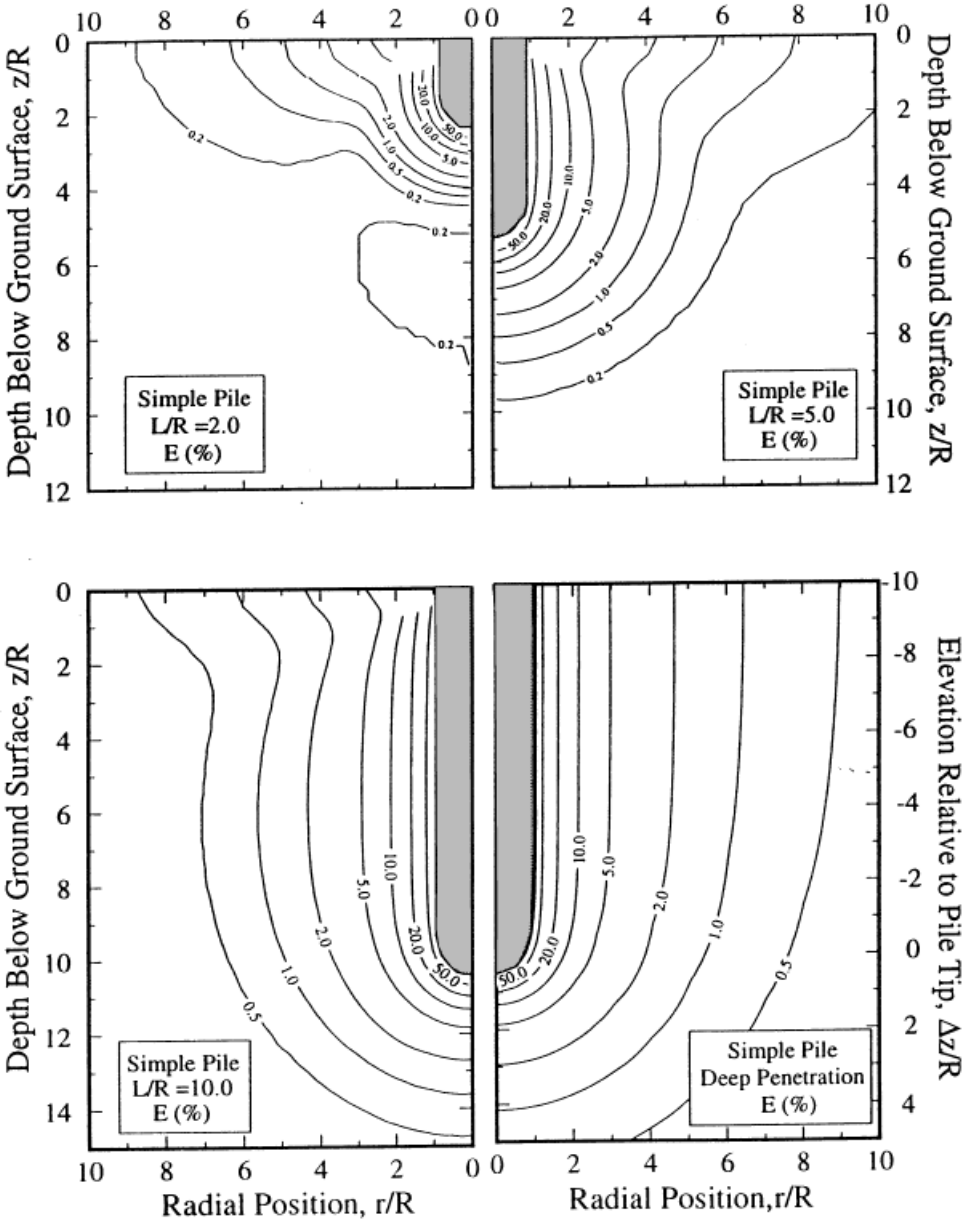

Figure 9. Contours of octahedral shear strain around simple pile

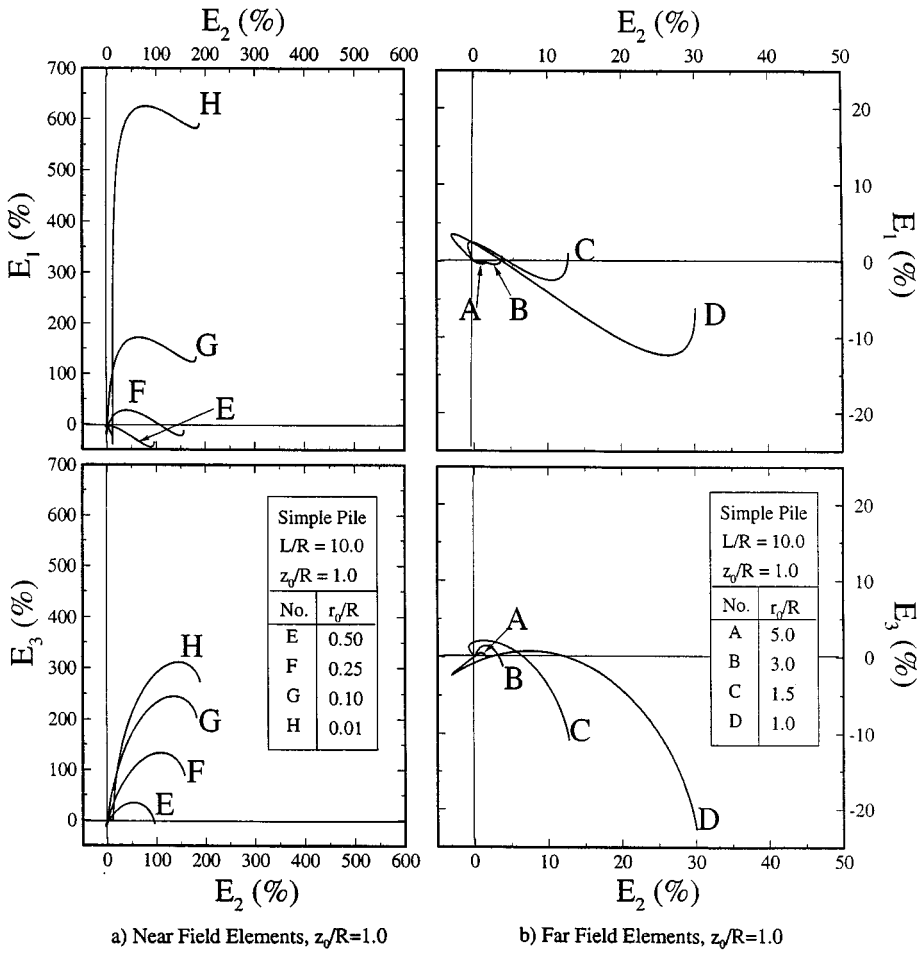

Figure 10. Strain paths around simple pile with $L/R = 10$

5. RESULTS FOR THE SIMPLE TUBE (OPEN-ENDED CAISSON)

Shallow Strain Path solutions for the simple tube geometry simulate the unplugged penetration of open-ended piles and caissons of specified aspect ratio, R/w. As in the previous section, the deformations and strains are solved by numerical integration of the velocity and strain rate expressions for large strains given in Appendix I. Surface displacements can be estimated at the centre of the tube ($r = 0, z = 0$) using small strain assumptions:

$$\delta_{r\mathrm{SS}}(0,0) = 0$$
$$\delta_{z\mathrm{SS}}(0,0) = -2wR\left(\frac{1}{R} - \frac{1}{\sqrt{R^2 + L^2}}\right) = -\frac{\Omega}{2\pi}\left(\frac{1}{R} - \frac{1}{\sqrt{R^2 + L^2}}\right) \tag{7}$$

where Ω is the cross-sectional area of the thin-walled tube ($\Omega = 4\pi wR$).

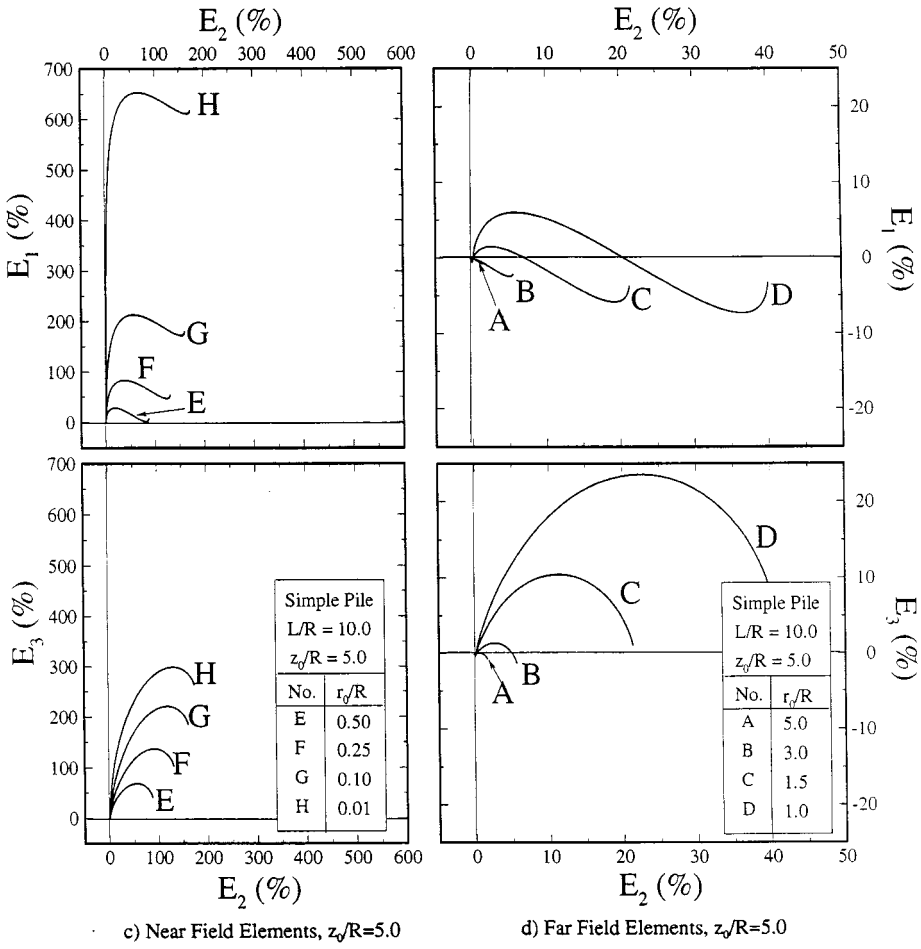

Figure 10. (*Continued*)

Comparing equation (7) with equation (5), it can be seen that the expression for the vertical displacement is the same, if the nominal tube radius, R, is equated with the radial distance, r. This means that the surface heave at the centre of an open-ended pile of radius, R is the same as the heave at a distance R from the axis of a solid pile of the same cross-sectional area.

5.1. Simple tube geometry

Figure 11 shows the geometry of a thin-walled simple tube with aspect ratio, $R/w = 40$, generated by the proposed SSPM analysis at a penetration depth $L/R = 5$ ($L/w = 200$). The shaft of the simple tube is not perfectly straight, but instead the mean radius increases slightly moving from the tip towards the free surface. The radius increases from $R/w \approx 40{\cdot}0$ at the tip to $R/w = 40{\cdot}4$ over most of the shaft length and then flares out further to $R/w \approx 40{\cdot}7$ near the free

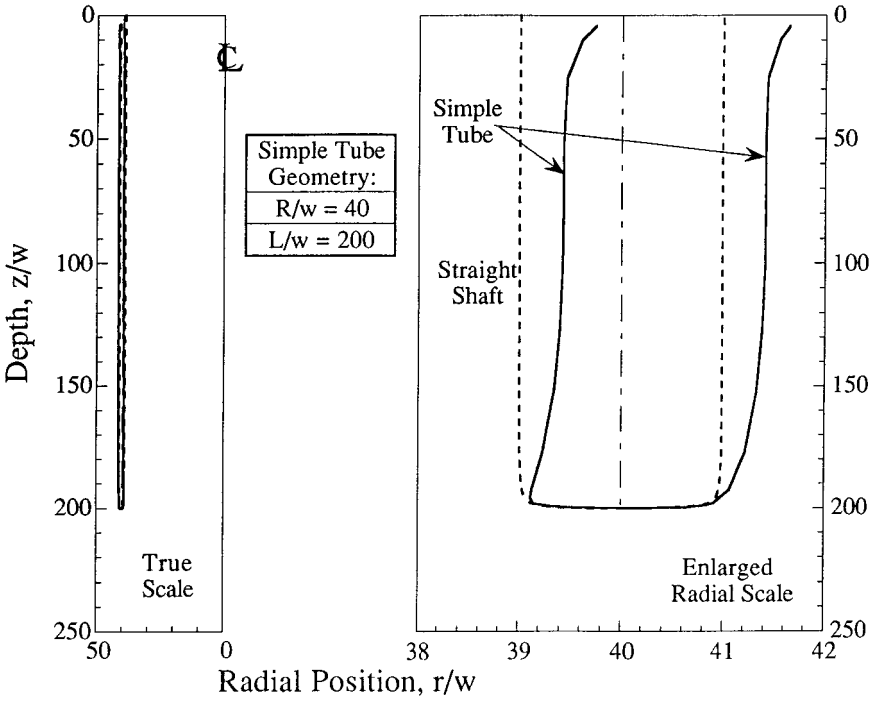

Figure 11. Wall shape of simple tube with aspect ratio, $R/w = 40$

surface. The wall itself is almost constant in thickness ($R_o - R_i \approx 2w$) over most of the shaft length.

Previous results of SPM analyses for deep penetration[10] also show continuous expansion of the simple tube with distance above the tip (location of the ring source). For deep penetration, the tube expansion approaches an asymptotic limit, $\Delta R/w = 0{\cdot}5$, referred to as the 'inherent clearance'.[4] These subtle details of the tube geometry have only a minor influence on the soil outside the tube, but can represent a significant factor in computing deformations and strains within the soil plug, especially for thick-walled tubes or long embedment to radius (L/R) ratios.

5.2. *Ground deformations*

Figure 12 illustrates the effects of the tube aspect ratio, R/w, on the deformations inside the soil plug. The figure compares the vertical deformations of a shallow plane (initially located at $z_0/w = 8$) caused by the penetration of simple tube penetrometers with aspect ratios, $R/w = 10, 20$ and 40, which are all embedded to a depth, $L/w = 80$. The results for the simple wall ($R/w = \infty$) are also shown for comparison. Apart from a very thin annulus of soil adjacent to the walls of the tube, which is dragged downward during penetration, the rest of the surface shows a net heave. The surface heave is non-uniform and varies radially across the plug. It is maximum close to the inside wall of the tube and is approximately proportional to the wall thickness, with very little influence of the tube radius (R/w) (i.e. $\delta_z/w = 1{\cdot}85$–$1{\cdot}95$ for all four cases). The

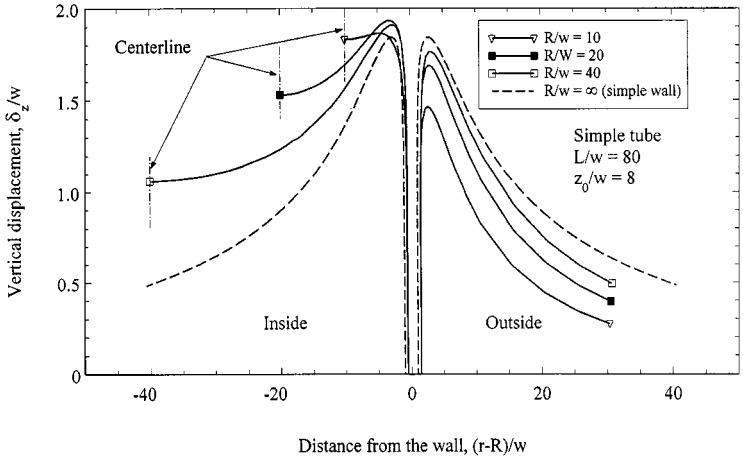

Figure 12. Effect of aspect ratio, R/w, on shallow deformations in the simple tube

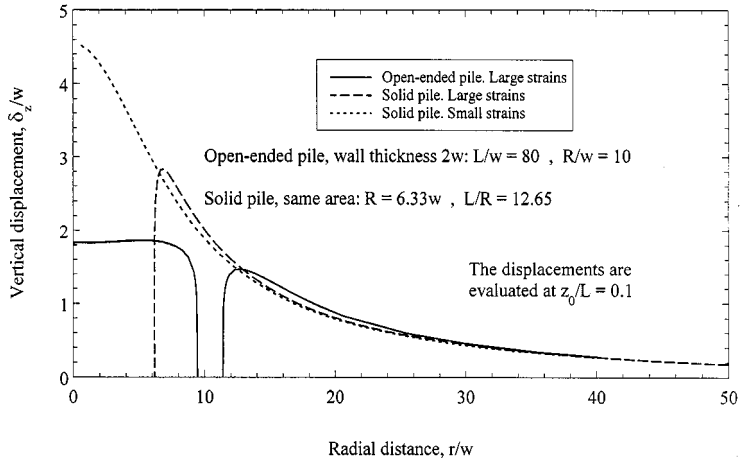

Figure 13. Comparison of shallow deformations in open-ended and solid piles

distribution of movements changes significantly with the aspect ratio. In contrast to the behaviour of the thin walled tube ($R/w = 40$), vertical displacements within the thick walled tube ($R/w = 10$) remain almost constant across the central portion of the soil plug. The maximum heave outside the caisson increases significantly with the aspect ratio, R/w, from 1·47 for $R/w = 10$ to 1·77 for $R/w = 40$, with the limit of 1·85 for the simple wall ($R/w = \infty$).

Figure 13 compares the ground deformations for the simple tube ($L/w = 80$, $R/w = 10$) with the case of a solid pile of the same cross-sectional area. The deformations outside the tube are almost identical in both cases, and coincide also with the small strains solution for the solid pile.

Figures 14(a) and 14(b) show contours of the radial and vertical displacements (δ_r/w and δ_z/w) caused by a simple tube ($R/w = 40$) with penetration depths, $L/R = 2$ and $L/R = 5$, respectively.

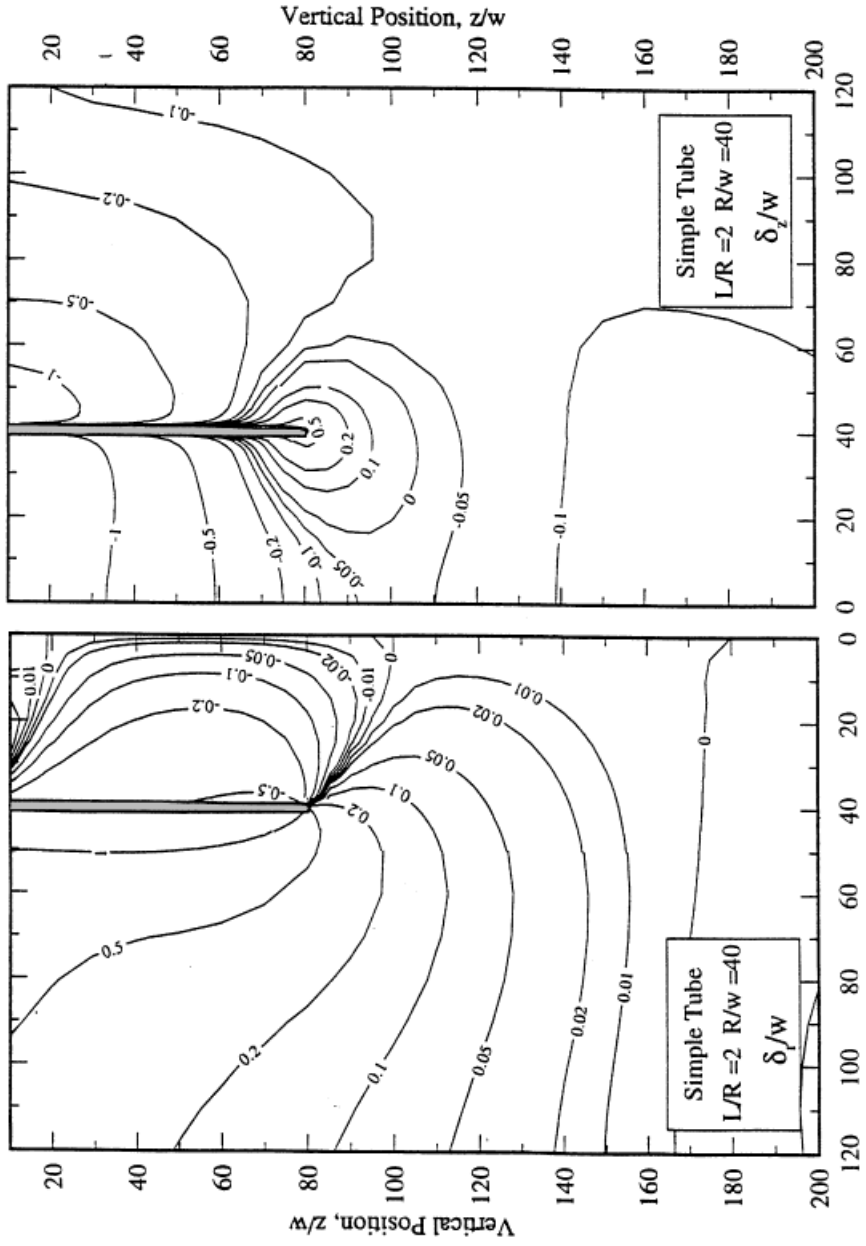

a) L/R=2

Figure 14. Displacement contours around simple tube with $R/w = 40$

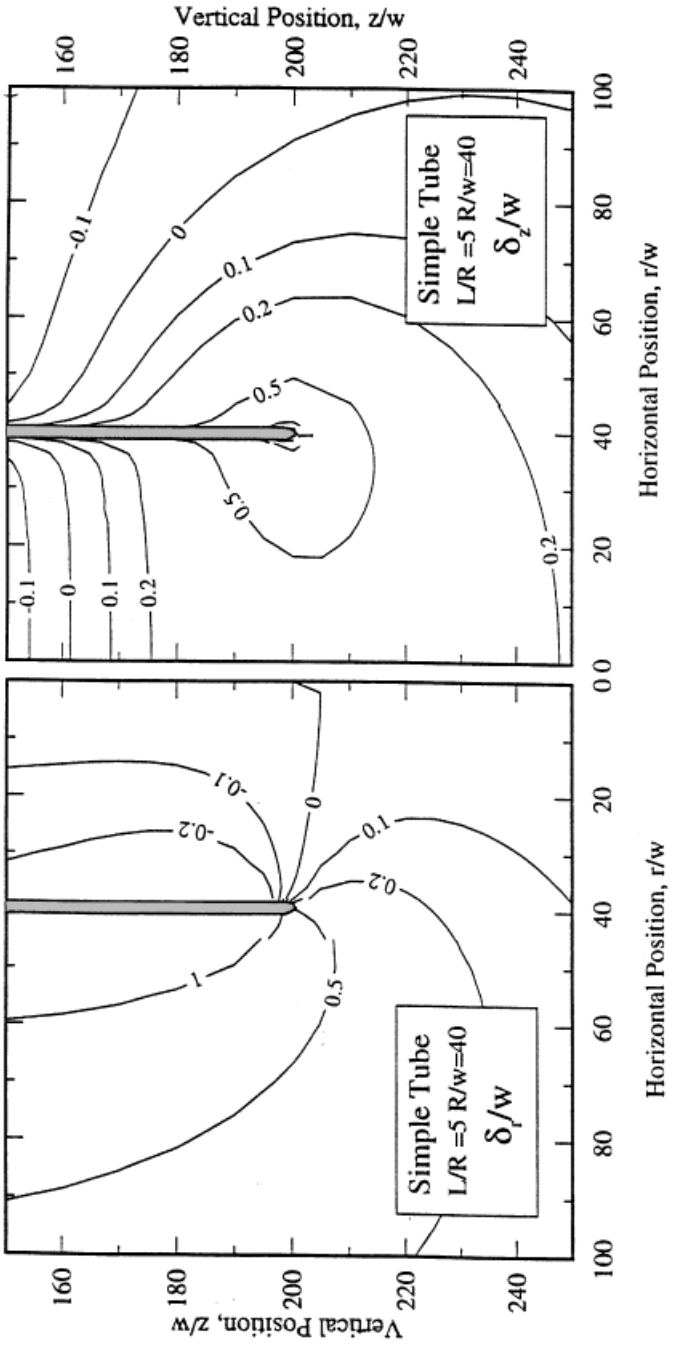

b) L /R=5

Figure 14. (*Continued*)

Most of the soil around the tube experiences net upward displacement ($\delta_z/w < 0$) Vertical deformations are relatively uniform across the pile plug over most of the embedded length of the tube. At any given depth, the heave is always larger inside the tube than outside.

As in the pile and wall cases, the zone of soil settlement comprises a thin veneer around the walls of the tube connecting to a bulb shaped region. For $L/R = 2$ (Figure 14(a)), this bulb extends to a depth $\Delta z/L \approx 0{\cdot}30$ below the tip of the tube (source elevation) with a maximum radial dimension of $\Delta r/\mathrm{L} \approx 0{\cdot}25$. These results are comparable to solutions presented previously for the simple wall geometry. When the tube penetrates to a depth $L/R = 5$ (Figure 14(b)), the settlement bulb expands across the entire base of the soil plug, extending outside the tube to a radius $\Delta r/L = 0{\cdot}3$ and vertically ahead of the tip (source elevation) $\Delta z/L = 0{\cdot}5$ (i,e. approaching the conditions for the solid simple pile geometry).

The contour of $\delta_r/w = 0$ delineates the zone of net inward soil movement and forms a locus which is similar to the geometry of an equivalent simple pile of radius R, and is largely independent of the embedment depth. All other points in the soil experience net outward movements ($\delta_r/w > 0$) with similar distribution to the simple pile, but with magnitudes controlled by the volume of soil displaced by the walls of the tube.

Figures 15(a) and 15(b) show the deformation paths of selected soil elements located close to the tube wall at four different initial depths $z_0/L = 0{\cdot}1, 0{\cdot}5, 0{\cdot}9$ and $1{\cdot}0$, as the tube penetrates from the surface to a total embedment depth $L/R = 2$, for elements which move inside and outside the tube, respectively. For the soil elements which are displaced outside the tube (Figure 15(b)), the radial displacements increase continuously with embedment depth (similar results for the simple pile were shown in Figure 8). For elements which move inside the tube (Figure 15(a)), there is a characteristic pattern of small outward displacements, which then reverse direction when the wall tip approaches the depth of the element. All elements inside the caisson have a net inward radial displacement. For elements initially located at $z_0/L = 0{\cdot}1, 0{\cdot}5$, there is a second reversal in the direction of the radial displacements and continuous outward movement with subsequent penetration of the tube. This behaviour is related to the inherent clearance of the simple tube geometry described above.

5.3. Shear strains

Figures 16(a) and 16(b) compare contours of the octahedral shear strain, E, for shallow penetration of the thin-walled simple tube ($R/w = 40$) at a depth $L/R = 2{\cdot}0$, with previous SPM solutions[10] for deep penetration (the elevations are reported relative to the wall tip).

For shallow penetration (Figure 16(a)), the zone of intense soil shearing ($E \geqslant 10\%$) is restricted to a thin annulus around the wall of the tube (with characteristic dimension comparable to w). All points inside the soil plug undergo significant amounts of shearing ($E \geqslant 1\%$). Outside the tube, the zone of intermediate strains ($0{\cdot}1 \leqslant E \leqslant 10\%$), extends radially to $\Delta r/w \approx 150$ and a similar distance below the wall tip. At points in the exterior region around the wall of the tube, all soil elements undergo monotonically increasing levels of shear strain with continued penetration (i.e. similar to conditions around the simple pile).

A comparison of the two analyses (Figures 16(a) and 16(b)) shows that the zone of intense shearing ($E \geqslant 10\%$) is largely unaffected by the embedment depth and is controlled by the wall thickness. However, the embedment depth does affect the extent of the zone of intermediate strains levels, both around the outside of the tube and in the region below the wall tip. It is very difficult to compare the strain levels inside the soil plug due to reversals in the magnitude of

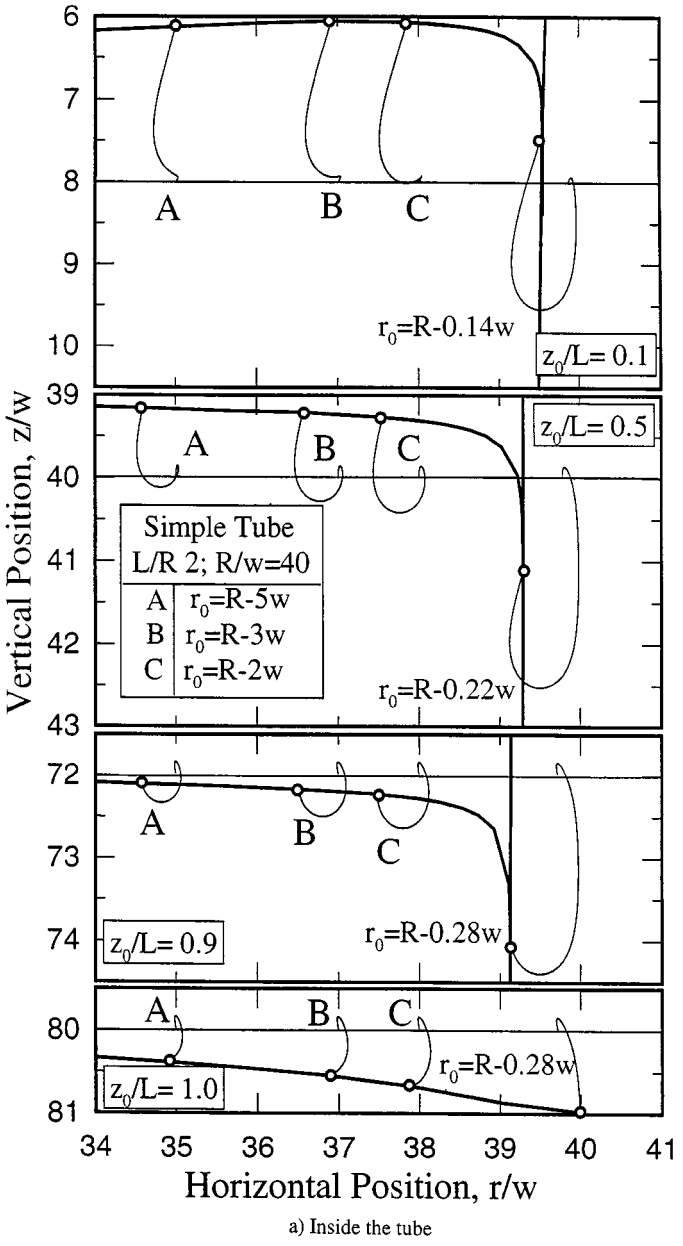

Figure 15. Deformation paths around simple tube with $R/w = 40$ and $L/R = 2$

E predicted in the deep penetration analyses. The results in Figure 16(b) imply that most of the soil elements within the tube ($r/w \leqslant 30$) experience maximum shear strains, $E \leqslant 1\%$ while they are still below the tip of the penetrating tube. After reaching a local minimum strain close to the tip elevation, subsequent strains inside the soil plug are largely controlled by the inherent

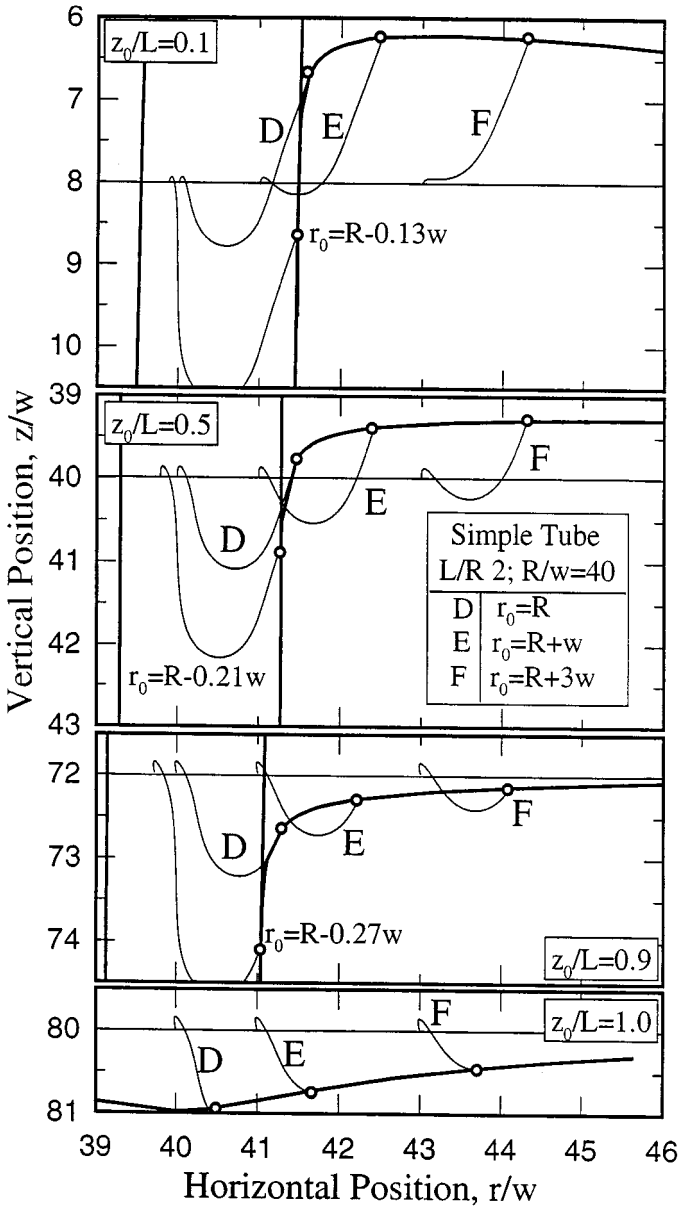

b) Outside the tube

Figure 15. (*Continued*)

clearance of the simple tube geometry. In contrast, the shallow penetration analysis (Figure 16(a)) predicts larger shear strains throughout the soil plug, whose distribution is clearly related to the deformations occurring at the stress free ground surface (cf. Figure 12).

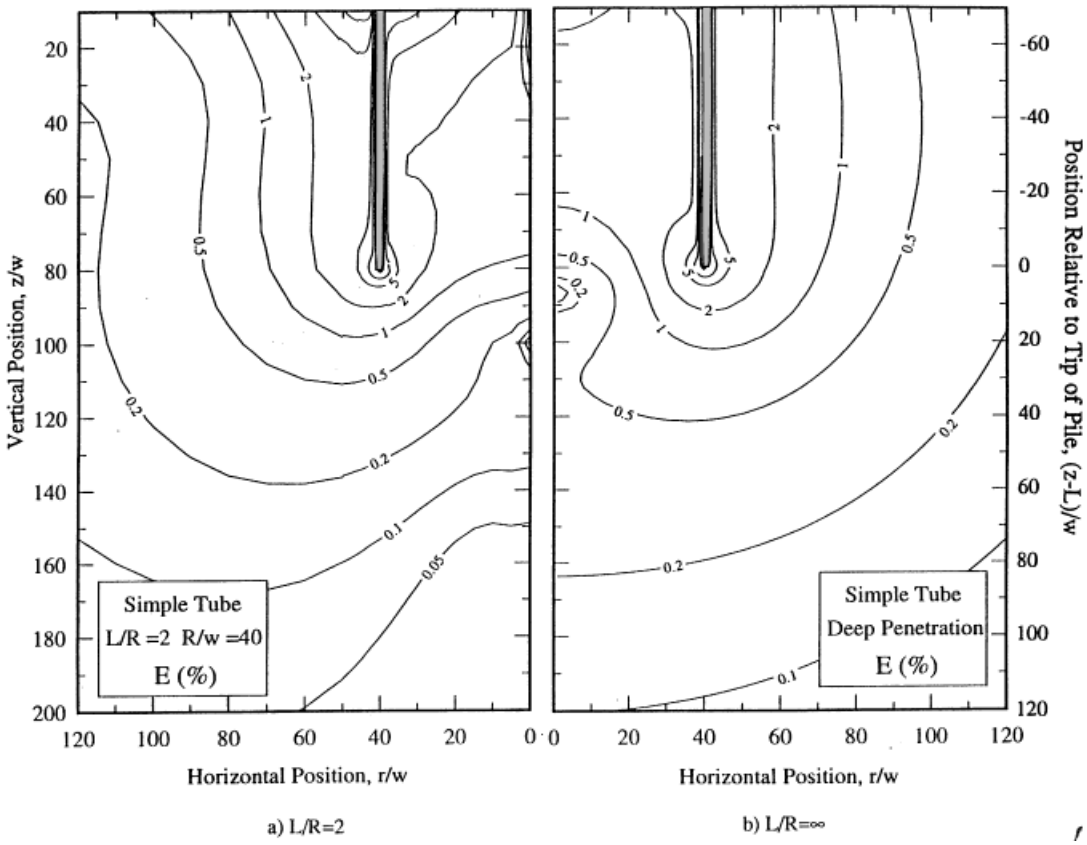

Figure 16. Contours of octahedral shear strain around simple tube with $R/w = 40$

At points along the axis of the caisson, soil elements are subject to undrained triaxial shearing, with $\varepsilon_{rr} = -1/2\varepsilon_{zz}$. Figure 17 shows the vertical strains at selected elevations along the centerline as the tube penetrates from the surface to a total embedment depth, $L/w = 80$. The soil element at $z_0/w = 40$ is initially sheared in triaxial compression, reaching a maximum vertical strain $e_{zz} \approx 0{\cdot}4\%$ when the tube tip penetrates to a depth $h/w = 15$ (i.e. the point is still at a distance $\Delta z/w = 25$ below the tip). As penetration continues, the direction of shearing reverses to one of triaxial extension which continues as the tip moves past the elevation of the soil element, reaching a maximum strain in extension of $e_{zz} \approx -1{\cdot}75\%$ at $h/R \approx 70$. Thereafter, the axial strain again increases (compression mode). At points closer to the free surface ($z_0/w = 30, 20$), the tendency to develop compressive strains when $z_0/h \ll 1$ (i.e. when the point is inside the tube) becomes even more pronounced. This behaviour is again directly related to the inherent clearance exhibited by the simple tube.

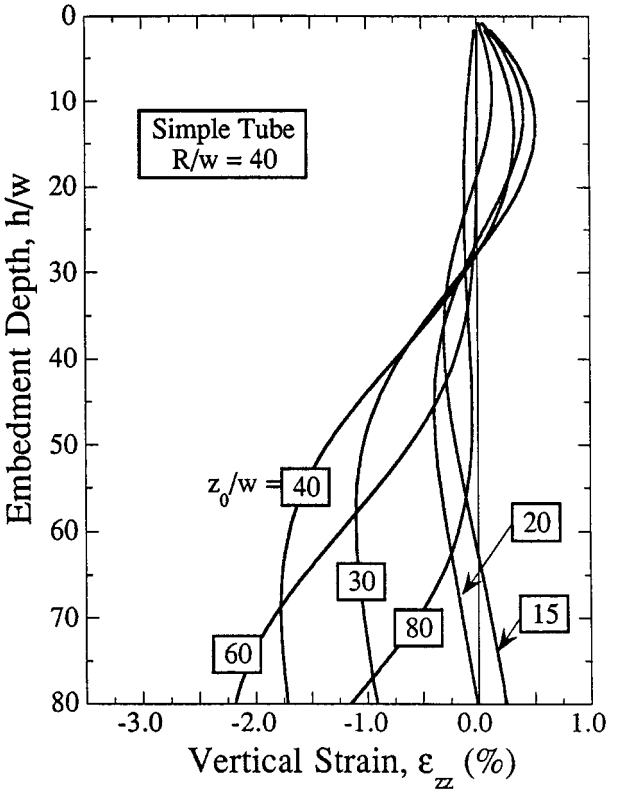

Figure 17. Vertical strain at the centreline of simple tube with $R/w = 40$ and $L/R = 2$

6. CONCLUSIONS

This paper has described a new method for estimating the deformations and strains caused by shallow, undrained penetration of plane strain and axisymmetric piles and caissons in clay. The formulation combines the strain path method developed by Baligh[1] for analysis of deep penetration in clays, with the work of Sagaseta[2] for estimating deformations near the stress-free ground surface. The proposed formulation, referred to as the Shallow Strain Path Method (SSPM), simulates the penetration process using the method of sources and sinks (potential theory) and satisfies the stress boundary conditions at the free surface through a distribution of corrective surface tractions (solved by linear, isotropic elastic theory). The analyses provide complete solutions for the velocity and strain rate components at any selected point within the soil. Deformations and strains can then be obtained by integrating along the particle path as functions of the penetrometer embedment depth. Appendix I gives complete solutions for three penetrometer geometries (plane strain) wall, axisymmetric simple pile, and simple tube. The analyses give partial representation of large strain conditions close to the surface of the penetrometer, while small strain approximations can provide useful analytic expressions for deformations.

The results illustrate the transition from shallow to deep penetration. For the wall and simple pile geometries, shallow penetration causes heave at the ground surface, while settlements occur

only in the region around the tip and in a thin veneer of material adjacent to the shaft of the penetrometer. Downward movements of soil particles close to the shaft are associated with the representation of large strain conditions in the proposed SSPM analyses. The zone of settlement around the pile tip is related to the embedded length of the penetrometer, L. For the plane strain wall geometry, the settlement bulb has characteristic radius $\Delta r/L \approx 0{\cdot}3$, while $\Delta r/L \approx 0{\cdot}6$ for the axisymmetric simple pile geometry. Simple tube penetration also generates heave at the ground surface both within the soil plug and at points outside the tube. At shallow penetration, the settlement bulb around the tube resembles the behaviour of the simple wall, while at larger embedment depths settlements occur at all points below the tip of the tube, and approach the conditions for a closed-ended (simple) pile of radius R.

The geometry of the simple pile corresponds to a round-tipped closed-ended circular-section pile, with a straight cylindrical shaft that tapers at points close to the free surface. Further improvements in modelling the geometry of a real pile shaft are only required for points close to the free surface (at depths $z/R \leqslant 1$). In contrast, deformations inside an open-ended pile/caisson are affected significantly by the 'inherent clearance' of the simple tube geometry.

Further research on the SSPM analyses should focus in combining the SPPM solutions with constitutive models of soil behaviour and equilibrium conditions to estimate the stress and pore pressure field caused by shallow penetration in clays.[15,16,20] A comparison with actual observations in the laboratory and in the field is under preparation.[8,21]

ACKNOWLEDGEMENTS

This research has been partially supported by Grant No. 93-204 of DGICYT, Spain, covering the visit of the first author to the Massachusetts Institute of Technology. The second and third authors received support from a Joint Oil Industry Consortium through a project entitled "Performance of Suction Caisson Foundations". The authors would also like to thank Twarath (John) Sutabutr for his help in preparing the figures.

APPENDIX I

The velocities and strain rates are given as the sum of three components: (1) source, (2) image sink, and (3) corrective surface tractions.

I.1. Simple wall

Velocities and strain rates at a point $P(x, z)$:

Step 1. Line source at $S(0, h)$:

$$v_{x1} = \frac{Uw}{\pi}\frac{x}{r_1^2}, \qquad v_{z1} = \frac{Uw}{\pi}\frac{z-h}{r_1^2} \tag{8a}$$

$$\dot{\varepsilon}_{xx1} = -\frac{Uw}{\pi}\frac{1}{r_1^2}\left(1 - 2\frac{x^2}{r_1^2}\right), \qquad \dot{\varepsilon}_{zz1} = -\dot{\varepsilon}_{xx1}$$

$$\dot{\varepsilon}_{xz1} = 2\frac{\mathrm{U}w}{\pi}\frac{1}{r_1^2}\left(1 - 2\frac{x(z-h)}{r_1^2}\right) \tag{8b}$$

where r_1 is the distance from the point $P(x,z)$ to the source $S(0,h)$:

$$r_1 = \sqrt{x^2 + (z-h)^2} \tag{9}$$

Step 2. Image line sink at $S'(0, -h)$:

$$v_{x2} = -\frac{Uw}{\pi}\frac{x}{r_2^2}, \qquad v_{z2} = -\frac{Uw}{\pi}\frac{z+h}{r_2^2} \tag{10a}$$

$$\dot{\varepsilon}_{xx2} = \frac{Uw}{\pi}\frac{1}{r_2^2}\left(1 - 2\frac{x^2}{r_2^2}\right), \qquad \dot{\varepsilon}_{zz2} = -\dot{\varepsilon}_{xx2}$$

$$\dot{\varepsilon}_{xz2} = 2\frac{Uw}{\pi}\frac{1}{r_2^2}\left(1 - 2\frac{x(z+h)}{r_2^2}\right) \tag{10b}$$

where r_2 is the distance from the point $P(x,z)$ to the sink $S'(0, -h)$:

$$r_2 = \sqrt{x^2 + (z+h)^2} \tag{11}$$

Step 3. Corrective surface shear tractions:

$$v_{x3} = 2\frac{Uw}{\pi}\frac{x}{r_2^2}\left[1 - 2\frac{z(z+h)}{r_2^2}\right] \qquad v_{z3} = -2\frac{Uw}{\pi}\frac{z}{r_2^2}\left(1 - 2\frac{x^2}{r_2^2}\right) \tag{12a}$$

$$\dot{\varepsilon}_{xx3} = -2\frac{Uw}{\pi}\frac{1}{r_2^2}\left[\left(1 - 2\frac{x^2}{r_2^2}\right)\left(1 - 2z\frac{z+h}{r_2^2}\right) + 4x^2 z\frac{z+h}{r_2^4}\right]$$

$$\dot{\varepsilon}_{zz3} = -\dot{\varepsilon}_{xx3} \tag{12b}$$

$$\dot{\varepsilon}_{xz3} = 2\frac{Uw}{\pi}\frac{1}{r_2^2}\frac{2x}{r_2^2}\left[h + 2z\frac{x^2 - (z+h)^2}{r_2^2}\right]$$

I.2. Simple pile

Velocities and strain rates at a point $P(r,z)$:

Step 1. Point source at $S(0,h)$:

$$v_{r1} = \frac{UR^2}{4}\frac{r}{r_1^3}, \qquad v_{z1} = \frac{UR^2}{4}\frac{z-h}{r_1^3} \tag{13a}$$

$$\dot{\varepsilon}_{rr1} = -\frac{UR^2}{4}\frac{1}{r_1^3}\left(1 - 3\frac{r^2}{r_1^2}\right) \qquad \dot{\varepsilon}_{\theta\theta 1} = -\frac{UR^2}{4}\frac{1}{r_1^3} \tag{13b}$$

$$\dot{\varepsilon}_{zz1} = -(\dot{\varepsilon}_{rr1} + \dot{\varepsilon}_{\theta\theta 1}) \qquad \dot{\varepsilon}_{rz1} = \frac{UR^2}{4}\frac{1}{r_1^3}\frac{3r(z-h)}{r_1^2}$$

where r_1 is the distance from the point $P(r,z)$ to the source $S(0,h)$:

$$r_1 = \sqrt{r^2 + (z-h)^2} \tag{14}$$

Step 2. Image point sink at $S'(0, -h)$:

$$v_{r2} = -\frac{UR^2}{4}\frac{r}{r_2^3}, \qquad v_{z2} = -\frac{UR^2}{4}\frac{z+h}{r_2^3} \tag{15a}$$

$$\dot{\varepsilon}_{rr2} = \frac{UR^2}{4}\frac{1}{r_2^3}\left(1 - 3\frac{r^2}{r_2^2}\right) \qquad \dot{\varepsilon}_{\theta\theta 2} = \frac{UR^2}{4}\frac{1}{r_2^3}$$

$$\dot{\varepsilon}_{zz2} = -(\dot{\varepsilon}_{rr2} + \dot{\varepsilon}_{\theta\theta 2}) \qquad \dot{\varepsilon}_{rz2} = -\frac{UR^2}{4}\frac{1}{r_2^3}\frac{3r(z+h)}{r_2^2} \tag{15b}$$

where r_2 is the distance from the point $P(r, z)$ to the source $S'(0, -h)$:

$$r_2 = \sqrt{r^2 + (z+h)^2} \tag{16}$$

Step 3. Corrective surface shear tractions:

$$v_{r3} = \int_0^\infty I_r(r, z, a) F_{\gamma SP}(a)\,\mathrm{d}a, \qquad v_{z3} = \int_0^\infty I_z(r, z, a) F_{\gamma SP}(a)\,\mathrm{d}a \tag{17a}$$

$$\dot{\varepsilon}_{rr3} = \int_0^\infty \frac{\partial I_r}{\partial r} F_{\gamma SP}\,\mathrm{d}a, \qquad \dot{\varepsilon}_{\theta\theta 3} = -\frac{1}{r}\int_0^\infty I_r F_{\gamma SP}\,\mathrm{d}a$$

$$\dot{\varepsilon}_{zz3} = -(\dot{\varepsilon}_{rr3} + \dot{\varepsilon}_{\theta\theta 3}), \qquad \dot{\varepsilon}_{rz3} = -\frac{1}{2}\int_0^\infty \left(\frac{\partial I_r}{\partial z} + \frac{\partial I_z}{\partial r}\right) F_{\gamma SP}\,\mathrm{d}a \tag{17b}$$

where the function $F_{\gamma SP}(a)$ gives the shear strain rate produced at a point M of the free surface at a radial distance, a, from the centreline by the combined effect of the source and the sink (Step 3(a)). For the simple pile, $F_{\gamma SP}(a)$ is defined by

$$F_{\gamma SP}(a) = 3UR^2\frac{ha}{r_h^5} \tag{18}$$

where r_h is the distance from the source $S(0, h)$ to the surface points $M(\pm a, 0)$, in the meridional plane:

$$r_h = \sqrt{a^2 + h^2} \tag{19}$$

The functions I_r and I_z in equations (17a) and (17b) are the elastic coefficients of influence for the displacements and strains at a point $P(r, z)$ due to a horizontal line load, p, acting along a ring of radius, a, on the surface of the elastic half-space (for the incompressible case, the elastic Poisson's ratio $\mu = 0{\cdot}5$):

$$\delta_r = \frac{p}{G} I_r(r, z, a), \qquad \delta_\theta = 0, \qquad \delta_z = \frac{p}{G} I_z(r, z, a) \tag{20a}$$

$$\varepsilon_{rr} = -\frac{p}{G}\frac{\partial I_r}{\partial r}, \qquad \varepsilon_{\theta\theta} = -\frac{1}{r}\frac{p}{G} I_r$$

$$\varepsilon_{zz} = -(\varepsilon_{rr} + \varepsilon_{\theta\theta}), \qquad \varepsilon_{rz} = -\frac{p}{G}\left(\frac{\partial I_r}{\partial z} + \frac{\partial I_z}{\partial r}\right) \tag{20b}$$

where the coefficients I_r and I_z were obtained by Sagaseta[2] by integrating Cerruti's solution for a horizontal point load:

$$I_r(r,z,a) = \frac{1}{2\pi}\left[A_{rK}\mathbf{K}(k) + A_{rE}\mathbf{E}(k)\right]$$
$$I_z(r,z,a) = \frac{1}{2\pi}\left[A_{zK}\mathbf{K}(k) + A_{zE}\mathbf{E}(k)\right] \tag{21}$$

The functions $K(k)$ and $E(k)$ are the complete elliptic integrals of the first and second kind, respectively:

$$\mathbf{K}(k) = \int_0^{\pi/2} \frac{\mathrm{d}\theta}{\sqrt{1-k^2\sin^2\theta}}, \qquad \mathbf{E}(k) = \int_0^{\pi/2} \sqrt{1-k^2\sin^2\theta}\,\mathrm{d}\theta \tag{22}$$

where $\eta = k^2 = 1 - r_{a1}^2/r_{a2}^2$ and r_{a1} and r_{a2} are the distances from the point $P(r,z)$ to the points $M(\pm a, 0)$, in the meridional plane:

$$r_{a1} = \sqrt{(a-r)^2 + z^2}; \qquad r_{a2} = \sqrt{(a+r)^2 + z^2} \tag{23}$$

and the coefficients:

$$A_{rK} = \frac{r_{a2}}{r}\left(1 - \frac{2ar - z^2}{r_{a2}^2}\right), \qquad A_{rE} = -\frac{r_{a2}}{r}\left[1 + \frac{z^2}{2}\left(\frac{1}{r_{a1}^2} + \frac{1}{r_{a2}^2}\right)\right]$$
$$A_{zK} = -\frac{z}{r_{a2}}, \qquad A_{zE} = \frac{z}{r_{a2}}\left[1 - \frac{2a(a-r)}{r_{a1}^2}\right] \tag{24a}$$

A.3. Simple tube

Velocities and strain rates at a point $P(r,z)$:

Step 1. Ring source of radius R centred at $S(0,h)$:

$$v_{r1} = \frac{UwR}{\pi}\left[A_{1rK}\mathbf{K}(k_1) + A_{1rE}\mathbf{E}(k_1)\right], \qquad v_{z1} = \frac{UwR}{\pi}\left[A_{1zE}\mathbf{E}(k_1)\right] \tag{25a}$$

$$\dot{\varepsilon}_{rr1} = -(\dot{\varepsilon}_{zz1} + \dot{\varepsilon}_{\theta\theta 1}), \qquad \dot{\varepsilon}_{\theta\theta 1} = -\frac{UwR}{\pi}\frac{1}{r}\left[A_{1rK}\mathbf{K}(k_1) + A_{1rE}\mathbf{E}(k_1)\right]$$
$$\dot{\varepsilon}_{zz1} = -\frac{UwR}{\pi}\left[-A_{1zE}\frac{1}{2\eta_1}\frac{\partial\eta_1}{\partial z}\mathbf{K}(k_1) + \left(\frac{\partial A_{1zE}}{\partial z} + A_{1zE}\frac{1}{2\eta_1}\frac{\partial\eta_1}{\partial z}\right)\mathbf{E}(k_1)\right] \tag{25b}$$
$$\dot{\varepsilon}_{rz1} = -\frac{UwR}{\pi}\left[-A_{1zE}\frac{1}{2\eta_1}\frac{\partial\eta_1}{\partial r}\mathbf{K}(k_1) + \left(\frac{\partial A_{1zE}}{\partial r} + A_{1zE}\frac{1}{2\eta_1}\frac{\partial\eta_1}{\partial r}\right)\mathbf{E}(k_1)\right]$$

where the parameter k_1 is given by

$$\eta_1 = k_1^2 = 1 - r_{11}^2/r_{12}^2 \tag{26}$$

r_{11} and r_{12} are the distances from the point $P(r, z)$ to the ring source $S(\pm R, h)$, in the meridional plane:

$$r_{11} = \sqrt{(r-R)^2 + (z-h)^2}; \qquad r_{12} = \sqrt{(r+R)^2 + (z-h)^2} \tag{27}$$

and

$$A_{1rK} = \frac{1}{r_{12}} \frac{1}{r}, \quad A_{1rE} = -\frac{1}{r_{12}} \left(\frac{1}{r} - 2 \frac{r-R}{r_{11}^2} \right), \quad A_{1zE} = \frac{1}{r_{12}} 2 \frac{z-h}{r_{11}^2} \tag{28}$$

Step 2. Image ring sink of radius R centred at $S'(0, -h)$:

$$v_{r2} = -\frac{UwR}{\pi} [A_{2rK}\mathbf{K}(k_2) + A_{2rE}\mathbf{E}(k_2)], \qquad v_{z2} = -\frac{UwR}{\pi} [A_{2zE}\mathbf{E}(k_2)] \tag{29a}$$

$$\dot{\varepsilon}_{rr2} = -(\dot{\varepsilon}_{zz2} + \dot{\varepsilon}_{\theta\theta 2}), \qquad \dot{\varepsilon}_{\theta\theta 2} = \frac{UwR}{\pi} \frac{1}{r} [A_{2rK}\mathbf{K}(k_2) + A_{2rE}\mathbf{E}(k_2)]$$

$$\dot{\varepsilon}_{zz2} = \frac{UwR}{\pi} \left[-A_{2zE} \frac{1}{2\eta_2} \frac{\partial \eta_2}{\partial z} \mathbf{K}(k_2) + \left(\frac{\partial A_{2zE}}{\partial z} + A_{2zE} \frac{1}{2\eta_2} \frac{\partial \eta_2}{\partial z} \right) \mathbf{E}(k_2) \right] \tag{29b}$$

$$\dot{\varepsilon}_{rz2} = \frac{UwR}{\pi} \left[-A_{2zE} \frac{1}{2\eta_2} \frac{\partial \eta_2}{\partial r} \mathbf{K}(k_2) + \left(\frac{\partial A_{2zE}}{\partial r} + A_{2zE} \frac{1}{2\eta_2} \frac{\partial \eta_2}{\partial r} \right) \mathbf{E}(k_2) \right]$$

where the parameter k_2 is given by

$$\eta_2 = k_2^2 = 1 - r_{21}^2 / r_{22}^2 \tag{30}$$

r_{21} and r_{22} are the distances from the point $P(r, z)$ to the ring sink $S'(\pm R, -h)$, in the meridional plane:

$$r_{21} = \sqrt{(r-R)^2 + (z+h)^2}; \qquad r_{22} = \sqrt{(r+R)^2 + (z+h)^2} \tag{31}$$

and

$$A_{2rK} = \frac{1}{r_{22}} \frac{1}{r}, \quad A_{2rE} = -\frac{1}{r_{22}} \left(\frac{1}{r} - \frac{2(r-R)}{r_{21}^2} \right), \quad A_{2zE} = \frac{1}{r_{22}} \frac{2(z+h)}{r_{21}^2} \tag{32}$$

Step 3. Corrective surface shear tractions:

$$v_{r3} = \int_0^\infty I_r(r, z, a) F_{\gamma \mathrm{ST}}(a)\, \mathrm{d}a, \qquad v_{z3} = \int_0^\infty I_z(r, z, a) F_{\gamma \mathrm{ST}}(a)\, \mathrm{d}a \tag{33a}$$

$$\dot{\varepsilon}_{rr3} = -\int_0^\infty \frac{\partial I_r}{\partial r} F_{\gamma \mathrm{ST}}\, \mathrm{d}a, \qquad \dot{\varepsilon}_{\theta\theta 3} = -\frac{1}{r} \int_0^\infty I_r F_{\gamma \mathrm{ST}}\, \mathrm{d}a$$

$$\dot{\varepsilon}_{zz3} = -\dot{\varepsilon}_{rr3} - \dot{\varepsilon}_{\theta\theta 3}, \qquad \dot{\varepsilon}_{rz3} = -\frac{1}{2} \int_0^\infty \left(\frac{\partial I_r}{\partial z} + \frac{\partial I_z}{\partial r} \right) F_{\gamma \mathrm{ST}}\, \mathrm{d}a \tag{33b}$$

where the influence coefficients I_r and I_z are given in equation (22). The function $F_{\gamma ST}(a)$ is defined for the simple tube as

$$F_{\gamma ST}(a) = 8\,\frac{UwR}{\pi}\,[A_{hK}\mathbf{K}(k_h) + A_{hE}\mathbf{E}(k_h)] \tag{34}$$

where the parameters k_h is given by

$$\eta_h = k_h^2 = 1 - r_{h1}^2/r_{h2}^2 \tag{35}$$

r_{h1} and r_{h2} are the distances in the meridional plane from the ring source $S(\pm R, h)$ to the surface points $M(\pm a, 0)$:

$$r_{h1} = \sqrt{(a-R)^2 + h^2}\,; \qquad r_{h2} = \sqrt{(a+R)^2 + h^2} \tag{36}$$

and the coefficients A_{hK} and A_{hE} are given by

$$\begin{aligned} A_{hK} &= -\frac{h}{r_{h1}^2 r_{h2}}\,\frac{1-\eta_h}{\eta_h}\left(\frac{a-R}{r_{h1}^2} - \frac{a+R}{r_{h2}^2}\right) \\ A_{hE} &= \frac{h}{r_{h1}^2 r_{h2}}\left[\frac{2(a-R)}{r_{h1}^2} + \frac{a+R}{r_{h2}^2} + \frac{1-\eta_h}{\eta_h}\left(\frac{a-R}{r_{h1}^2} - \frac{a+R}{r_{h2}^2}\right)\right] \end{aligned} \tag{37}$$

REFERENCES

1. M. M. Baligh, 'Strain path method', *J. Geotech. Eng. ASCE*, **111,** 1108–1136 (1985).
2. C. Sagaseta, 'Analysis of undrained soil deformation due to ground loss', *Géotechnique*, **37,** 301–320 (1987).
3. M. M. Baligh and J.-N. Levadoux, 'Pore pressure dissipation after cone penetration', *Res. Report R80-11*, Dept. Civil Eng., MIT, Cambridge, MA, 1980.
4. M. M. Baligh, A. S. Azzouz and C.-T. Chin, 'Disturbances due to 'ideal' tube sampling', *J. Geotech. Eng. ASCE*, **113,** 739–757 (1987).
5. A. J. Whittle, C. P. Aubeny, A. Rafalovich, C. C. Ladd and M. M. Baligh, 'Interpretation of in-situ tests in cohesive soils using rational methods', *Res. Report R91-01*, Dept. Civil Eng., MIT, Cambridge, MA, 1991.
6. K. H. Andersen, R. Dyvik, K. Schrøder, O. E. Hansteen and S. Bysveen, 'Field tests of anchors in clays II: Predictions and Interpretation', *J. Geotech. Eng. ASCE*, **119,** 1532–1549 (1993).
7. E. C. Clukey and M. J. Morrison, 'A centrifuge and analytical study to evaluate suction caissons for TLP applications in the Gulf of Mexico', *Design and Performance of Piles and Piers in Soil and Soft Rock ASCE*, 141–156 (1993).
8. C. Sagaseta, A. J. Whittle and M. Santagata, 'Deformation analysis of shallow penetration in saturated clay', *Res. Report R94-09*, Dept. Civil Eng., MIT, Cambridge, MA, 1995.
9. M. M. Baligh, 'Undrained deep penetration: I. Shear stresses', *Géotechnique*, **36,** 471–485 (1986).
10. C.-T. Chin, 'Open-ended pile penetration in saturated clays', *Ph.D. Thesis*, Dept. Civil Eng., MIT, Cambridge, MA, 1986.
11. A. S. Vesic, 'Bearing capacity of deep foundations to sand', *Stresses in Soils and Layered Systems*, *Highway Research Board*, (39) 112–153 (1963).
12. E. I. Robinsky and C. F. Morrison, 'Sand displacement and compaction around friction piles', *Can. Geotech. J.*, **1,** 81–93 (1964).
13. J-N. Levadoux and M. M. Baligh, 'Pore pressures in clays due to cone penetration', *Res. Report R80-15*, Dept. Civil Eng., MIT, Cambridge, MA, 1980.
14. A. E. Williamson, 'Use of a panel method to predict disturbance due to penetrometer installation in clays', *SM. Thesis*, Dept. Civil Eng., MIT, Cambridge, MA, 1989.
15. C-I. Teh, 'An analytical investigation of the cone penetration test', *Ph.D. Thesis*, Dept. Eng. Sci., University of Oxford, U.K., 1987.

16. C. P. Aubeny, 'Rational interpretation of in-situ tests in cohesive soils', *Ph.D. Thesis*, Dept. Civil Eng., MIT, Cambridge, MA, 1992.
17. C. D. F. Rogers and M. P. O'Reilly, 'Ground movements associated with pipe installation and tunnelling', *Proc. 10th E.C.S.M.F.E.*, Florence, Italy, vol. 2, 1991, pp. 907–910.
18. D. N. Chapman, 'Ground movements associated with trenchless pipelaying operations', *Ph.D. Thesis*, Loughborough Univ. of Technology, U.K., 1993.
19. Y. K. Chow and C. I. Teh, 'A theoretical study of pile heave', *Géotechnique*, **40,** 1–14 (1990).
20. M. M. Baligh, 'Undrained deep penetration: II. Pore pressures', *Géotechnique*, **36,** 487–501 (1986).
21. C. Sagaseta and A. J. Whittle, 'Evaluation of ground movements due to pile driving in clay', in preparation.

